1988

Creep rupture of copper bicrystals /

John Farris
Lehigh University

Creep Rupture of Copper Bicrystals

by

John Farris

A Thesis

Presented to the Graduate Committee

of Lehigh University

in Candidacy for the Degree of

Master in Science

in

Mechanical Engineering & Mechanics

Lehigh University

1988

This thesis is accepted and approved in partial fulfillment of the requirements for the degree of Master of Science.

7 July 1988
(Date)

Terry J. Delph
Terry J. Delph
Advisor

Fazil Erdogan
Fazil Erdogan
Chairman, Department of
Mechanical Engineering
& Mechanics

Table of Contents

Abstract 1

1. Introduction 2

2. Experimental Design 5

    2.1 Experimental Apparatus 5

    2.2 Description of Test Specimens 7

3. Error Estimates 29

    3.1 Uncertainty in the Failure Time Due to Uncertainty in the Applied Stress 29

    3.2 Uncertainty in the Failure Due to Variation in Temperature 32

    3.3 Uncertainty in the Failure Time Due Eccentric Loading 34

4. Results 41

    4.1 Failure Times 41

    4.2 Weibull Analysis 43

    4.3 Fracture Surfaces 45

    4.4 Image Analysis 51

5. Conclusions 53

References 55

Vita 57

List of Tables

Table 2.2.1	Total Rotation, Twist and Tilt Angles for Specimen A	21
Table 2.2.2	Components of the Rotation Axis Vector for Specimen A	22
Table 2.2.3	Total Rotation, Twist and Tilt Angles for Specimen B	23
Table 2.2.4	Components of the Rotation Axis Vector for Specimen B	24
Table 2.2.5	Total Rotation, Twist and Tilt Angles for Specimen C	25
Table 2.2.6	Components of the Rotation Axis Vector for Specimen C	26
Table 2.2.7	Final Total Rotation, Twist and Tilt Angles	27
Table 2.2.8	Final Rotation Axis Vectors	28
Table 3.1.1	Error in Failure Times Due to Uncertainty in the Applied Stress	32
Table 3.3.1	Results of Eccentric Loading Analysis	39
Table 3.3.2	Error Analysis Results	40
Table 4.1.1	Failure Times for Specimen Group A	41
Table 4.1.2	Failure Times for Specimen Group B	42
Table 4.1.3	Failure Times for Specimen Group C	42
Table 4.4.1	Weibull Parameters for Each Test Series	43

List of Figures

Figure 2.1.1	Two ATS Ovens	6
Figure 2.1.2	Disassembled Weight Train	8
Figure 2.1.3	Control Panel	9
Figure 2.2.1	Stereographic Projection of Top Crystal in Bicrystal A	12
Figure 2.2.2	Stereographic Projection of Bottom Crystal in Bicrystal A	13
Figure 2.2.3	Stereographic Projection of Top Crystal in Bicrystal B	14
Figure 2.2.4	Stereographic Projection of Bottom Crystal in Bicrystal B	15
Figure 2.2.5	Stereographic Projection of Top Crystal in Bicrystal C	16
Figure 2.2.6	Stereographic Projection of Bottom Crystal in Bicrystal C	17
Figure 4.2.1	Weibull Plot of Failure Time Data	44
Figure 4.3.1	Fracture Surface of Specimen A3	46
Figure 4.3.2	Fracture Surface of Specimen B7	47
Figure 4.3.3	Creep Cavities from Specimen B1	48
Figure 4.3.4	Creep Cavities from Specimen B1	49
Figure 4.3.5	Creep Cavities from Specimen C1	50
Figure 4.4.1	Weibull Plot of the Area of Cavities from Specimen A2	52

Abstract

Three series of replicated creep rupture tests were performed on identical copper bicrystal specimens. The failure times were recorded and analyzed. Also a detailed error analysis was performed.

From our error analysis we concluded that the experimental error could only account for a small fraction of the observed scatter in the failure times when creep cavitation was the dominant failure mode. The two parameter Weibull distribution was found to fit the failure time data for all three test series well. Finally the statistical distribution of the cavity areas on the fracture surfaces was also found to have a Weibull fit.

Chapter 1 Introduction

The process of creep rupture deserves extensive study because it is an important failure mode at high temperatures. Energy conversion devices, for example, operate at elevated temperatures for long periods of time and are therefore susceptible to creep rupture. Currently there is no accurate method of predicting the creep rupture lifetime. This situation leads to overly conservative designs and considerable anxiety about the safety of older components. In order to make reliable predictions of creep failure times, the creep rupture process must be better understood.

The formation and growth of cavities along the grain boundaries is thought to be the major factor responsible for the creep rupture process. Cavities nucleate along the grain boundary, grow, link up to form cracks and eventually lead to failure. Researchers studying this process have found considerable scatter in the time to failure data of uniaxial test specimens tested under nominally identical conditions. For instance, the results of Lister et al [1] and Rutman, Krause, and Kremer [2] has shown an order of magnitude scatter in this data.

Some researchers believe that this scatter is

entirely due to experimental error. Hayhurst [3] performed an error analysis on the experiments carried out by Rutman, Kraus, and Kremer [2] and concluded that the scatter in the failure time data could be accounted for by the variations in the test parameters. Moreover Hayhurst [3] found that most of the scatter in the failure time data was could be attributed to loading eccentricity. Another body of thought, however, holds that the creep rupture is an intrinsically probabilistic process. Garofalo et al[4], for example, conducted a series of well-controlled replicated tests which still indicated considerable variations in the time to failure data.

The goal of this research is to experimentally quantify the scatter in the creep rupture times. To achieve this goal, three groups of eight identical specimens were tested at three different stress levels. The replication of tests at the same stress level allows us to to quantify the scatter in the failure time data. Copper bicrystal specimens were used as test specimens because of their extremely simple grain boundary structure. More importantly, the times-to-failure of bicrystals are known to be much less sensitive to the applied stress than are polycrystalline specimens, whose failure times depend upon the applied stress according to

a Monkman-Grant law. Hence experimental deviations from the nominal stress may be expected to have much less influence in becrystals than in polycrystals. A detailed error analysis was performed to determine how much of the scatter in the failure time data was due to experimental error.

Chapter 2 Experimental Design

2.1 Experimental Apparatus

The experimental apparatus was designed to provide a well controlled system in which to conduct creep experiments. The apparatus consists of four subsystems: high temperature furnaces and retorts, temperature controllers, load trains and an argon gas delivery system. The four Series 3210 split furnaces were built by Applied Test Systems (ATS) of Butler, PA.. Two ovens are shown in figure 2.1.1. Each oven encloses a stainless steel retort and contains nichrome heating elements. The retorts are equipped with water cooled seals, and are capable of maintaining a controlled gaseous environment. The temperature of the ovens is controlled by an ATS Series 3823 proportional controller. A chromel/alumel thermocouple positioned in the retort a few millimeters from the gauge section of test specimen provides the input temperature to the controller. This system controls the oven temperature to within 1°C .

The load train is designed to apply a dead weight uniaxial load to the specimen. The specimen is gripped at both ends by miniature commercial tubing fittings. The fittings are attached to flexible stainless steel cables. The top cable terminates in a threaded rod which screws into the top of the oven. The bottom cable is pinned to a

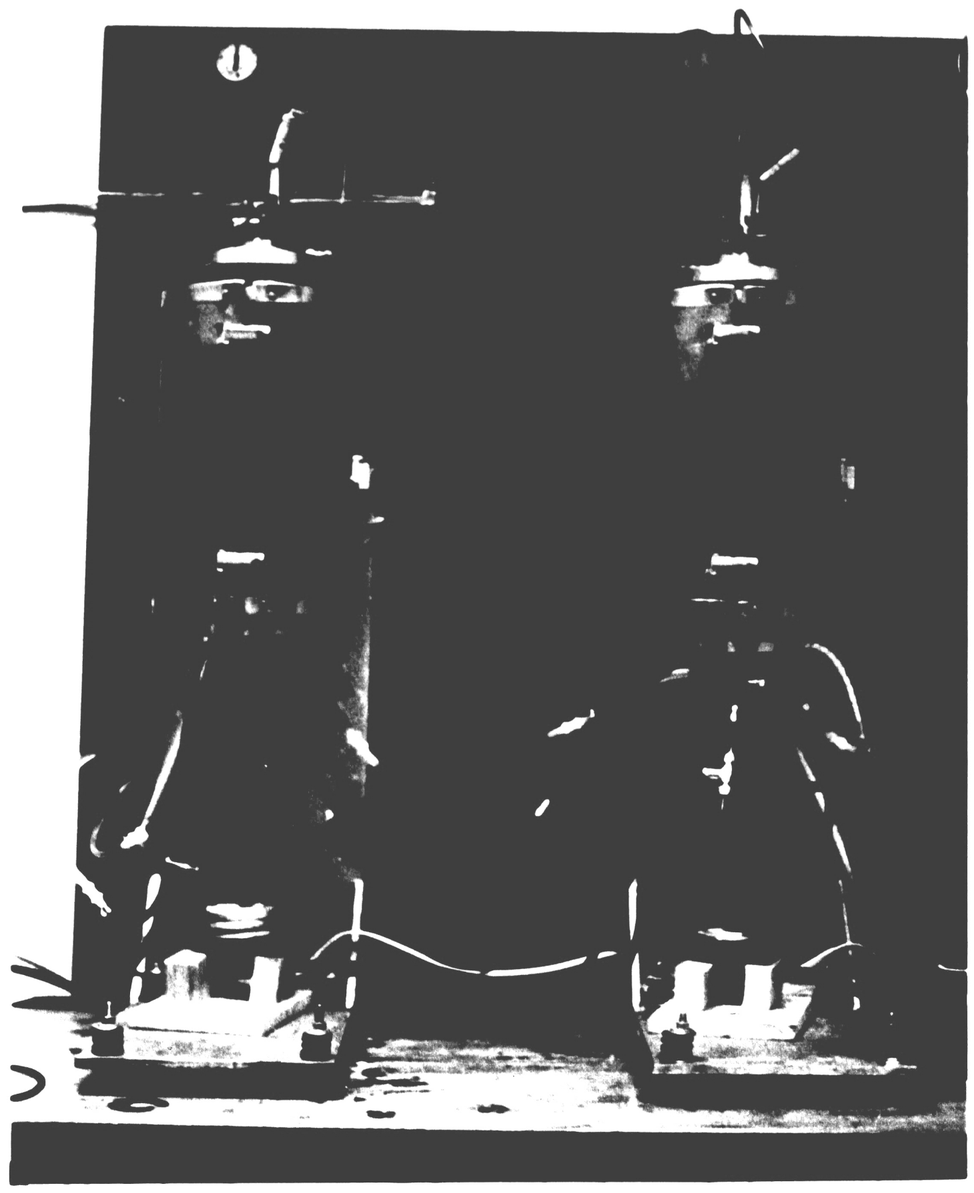

Figure 2.1.1 Two ATS ovens

pull rod which extends through the bottom of the oven and holds the weight pan. A disassembled weight train is shown in figure 2.1.2. Since the stainless steel cable cannot transmit a bending moment to the specimen, the only possible source of specimen bending is eccentric loading. A toggle switch is positioned below the weight pan. When the specimen breaks, the load pan falls on the switch, breaking a timing circuit and stopping a timing clock.

To prevent the copper specimen from oxidizing and to maintain a chemically inert environment, the retort is filled with argon gas and kept under 0.5 psig of pressure during the experiment. The argon gas is supplied from an industrial cylinder. A high pressure regulator reduces the pressure of the gas from the cylinders to 40 pounds per square inch. Then the argon flows through a molecular sieve where water vapor is removed from the gas. Next a low pressure regulator steps the pressure down to a half pound per square inch. Finally the flow is split into four different paths and routed to each oven. The regulators and control valves are mounted on a control panel as pictured in figure 2.1.3.

2.2 Description of the Test Specimens

The specimens tested were bicrystals made from 99.99% pure copper, grown from a melt using the Bridgeman technique. Three large bicrystals were fabricated in this

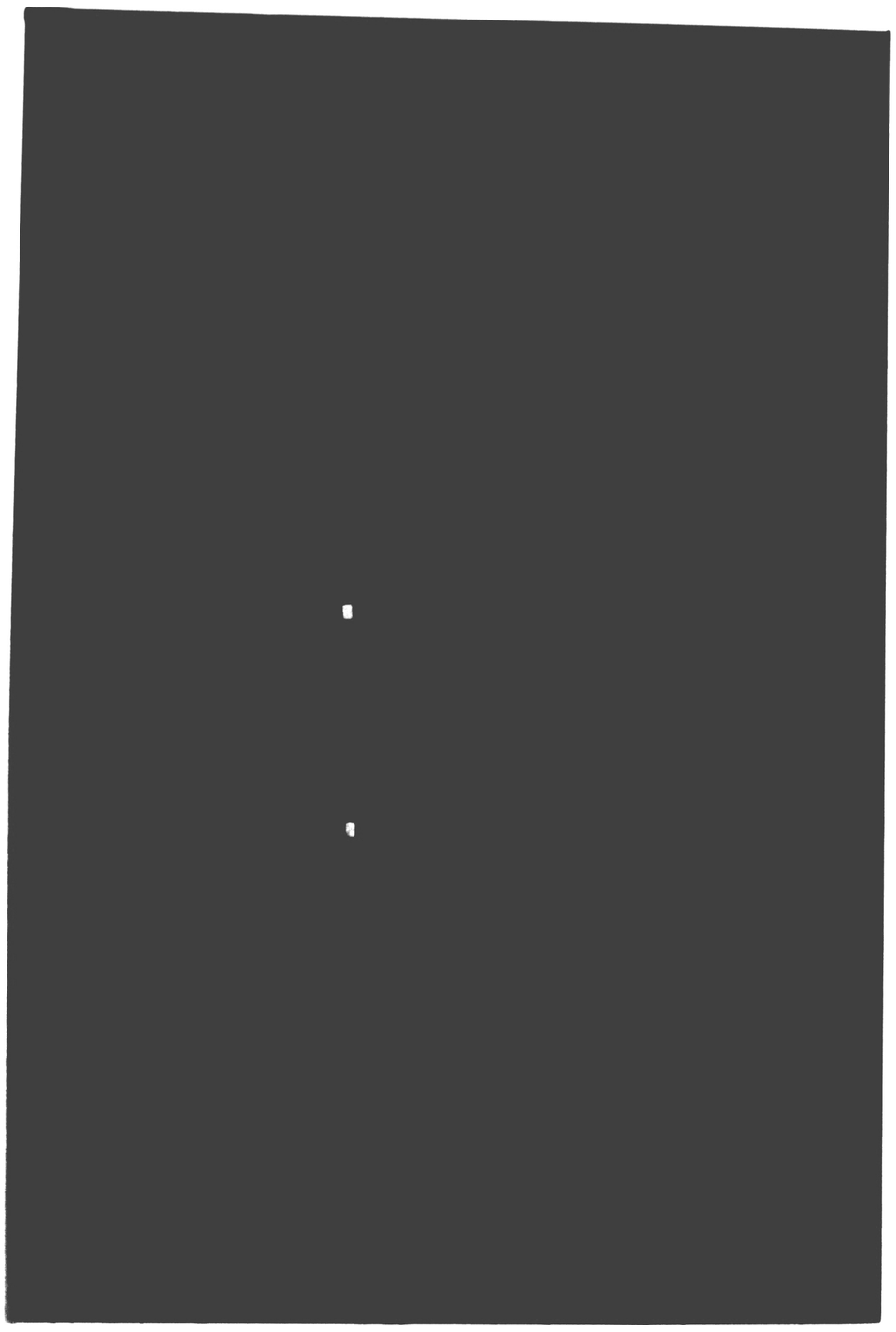

Figure 2.1.2 Disassembled weight train

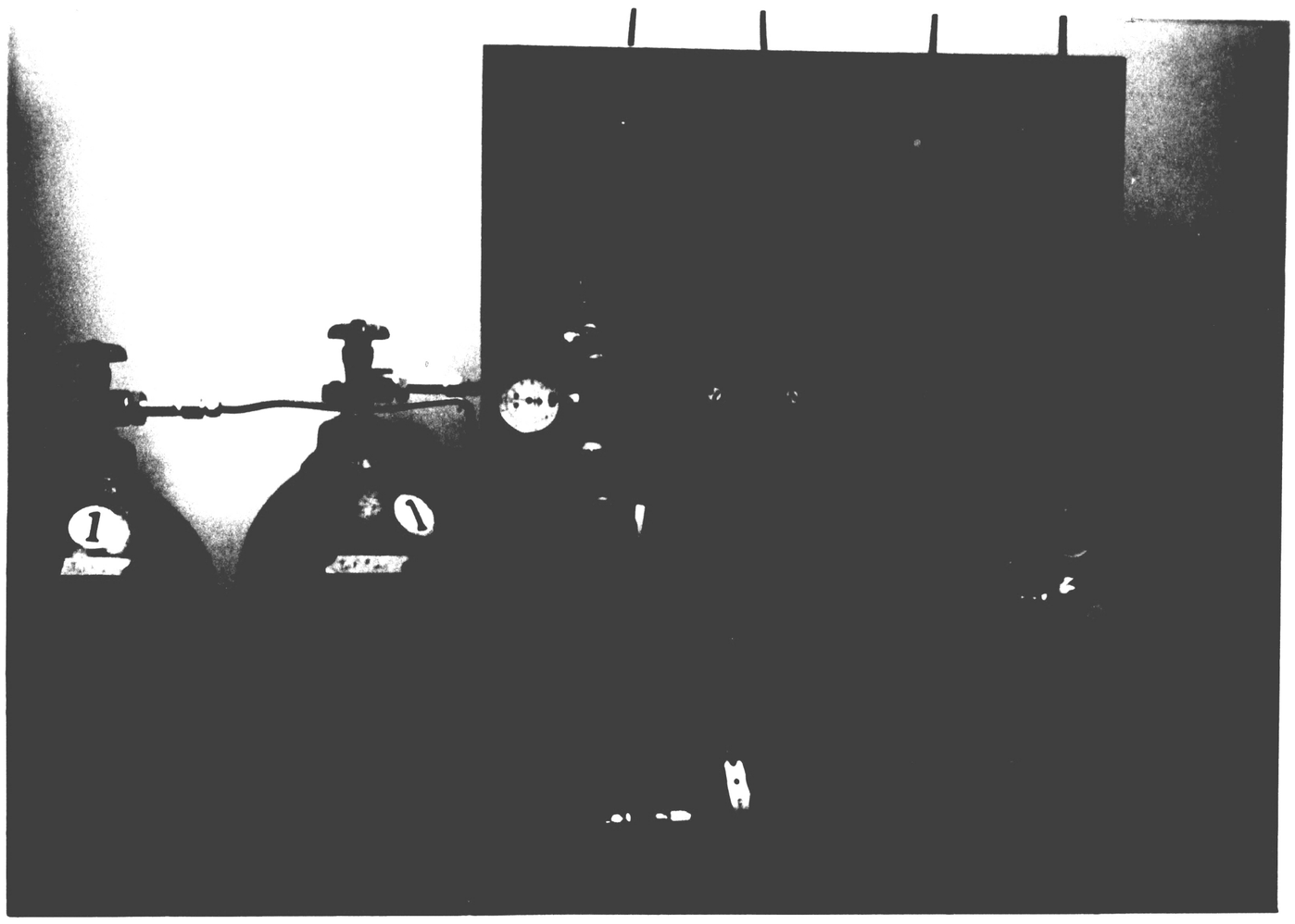

Figure 2.1.3 Control panel

manner. From each bicrystal, approximately 10 to 13 tensile specimens were cut using electrical discharge machining (EDM) techniques. The specimens had a gauge length of 1.5 inches and a gauge diameter of .25 inches. The grain boundary was orientated normal to the specimen axis and lay at the mid-section of the specimen. Three groups of eight specimens, each machined from a separate bicrystal, were designated as groups A, B and C and tested at different stress levels. The stress levels for groups A, B and C were 6.06 MPa, 2.13 MPa and 3.82 MPa, respectively.

To further characterize the specimens, the relative orientation of the two adjoining crystals in each bicrystal was determined. The amount of misorientation between two crystals can be described by a misorientation matrix [R]. The elements of [R] are the direction cosines of a coordinate axes aligned along the [100] axes of one crystal (bottom) with respect to a coordinate system aligned along the [100] axes of the other crystal (top). From the misorientation matrix we may derive the axis and angle of a rotation which would bring the two crystals in the bicrystal into alignment.

The back-reflection Laue method [5] was employed to determine the orientation of each crystal relative to a reference coordinate system. The stereographic

projections for each crystal are shown in figures 2.2.1 through 2.2.6. Following the procedure outlined by Lange [6], the misorientation matrix for the bicrystal was obtained using the relationship

$$[R] = [R_{bottom}]\ [R_{top}]^{-1}$$

where $[R_{top}]$ and $[R_{bottom}]$ are the misorientation matrices

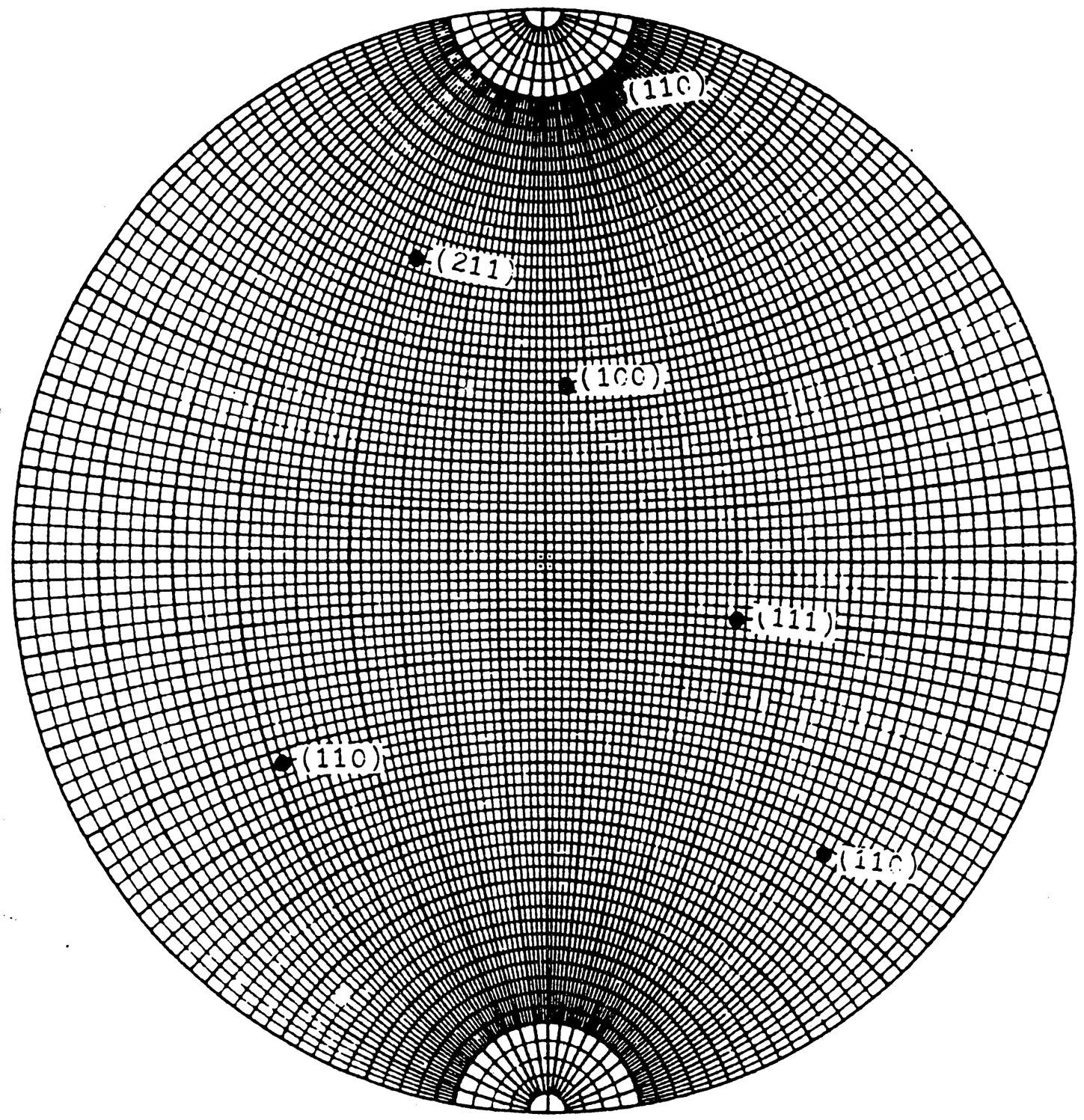

Figure 2.2.1 Stereographic projection of the top crystal in bicrystal A

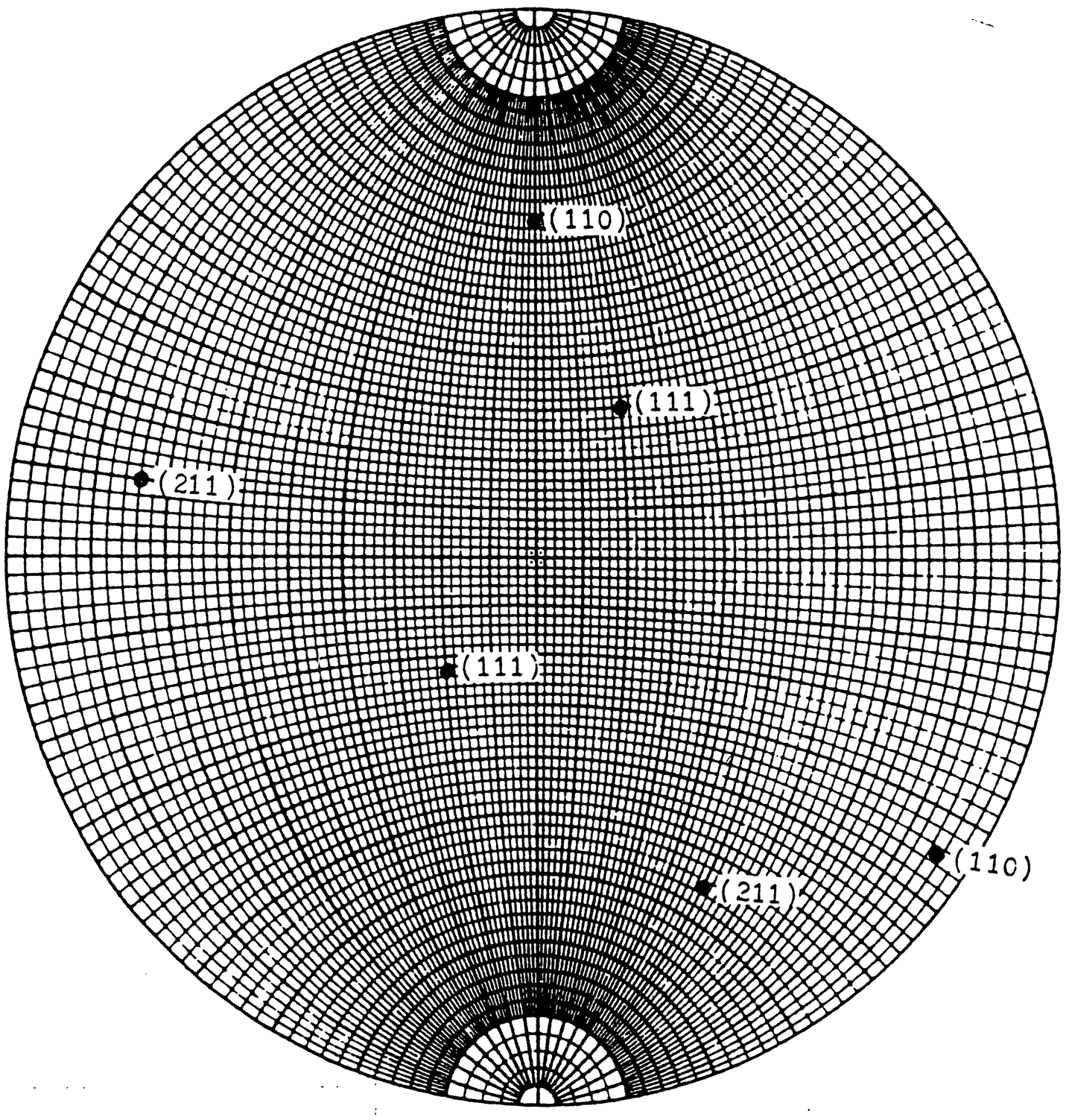

Figure 2.2.2 Stereographic projection of the bottom crystal in bicrystal A

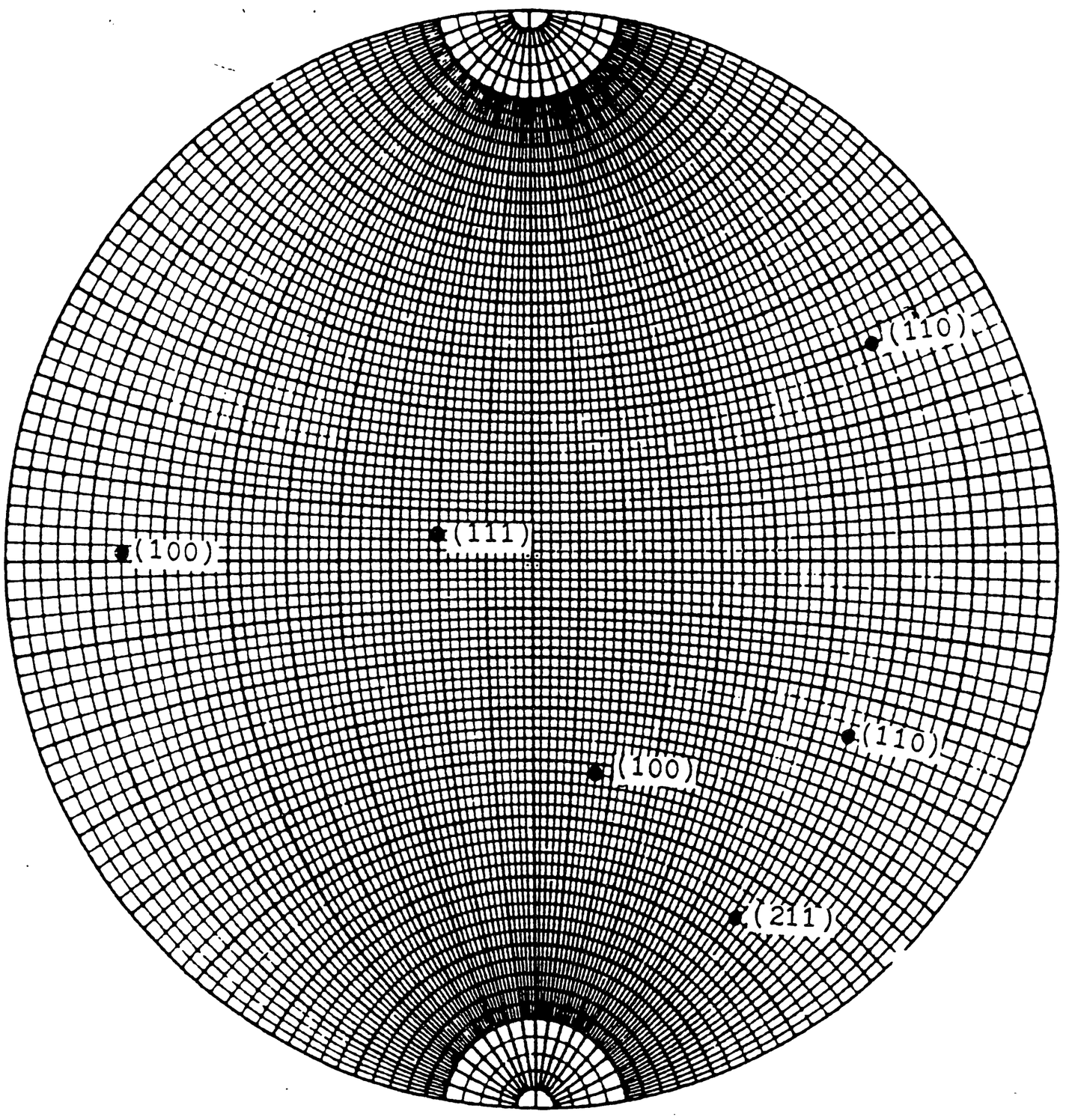

Figure 2.2.3 Stereographic projection of the top crystal in bicrystal B

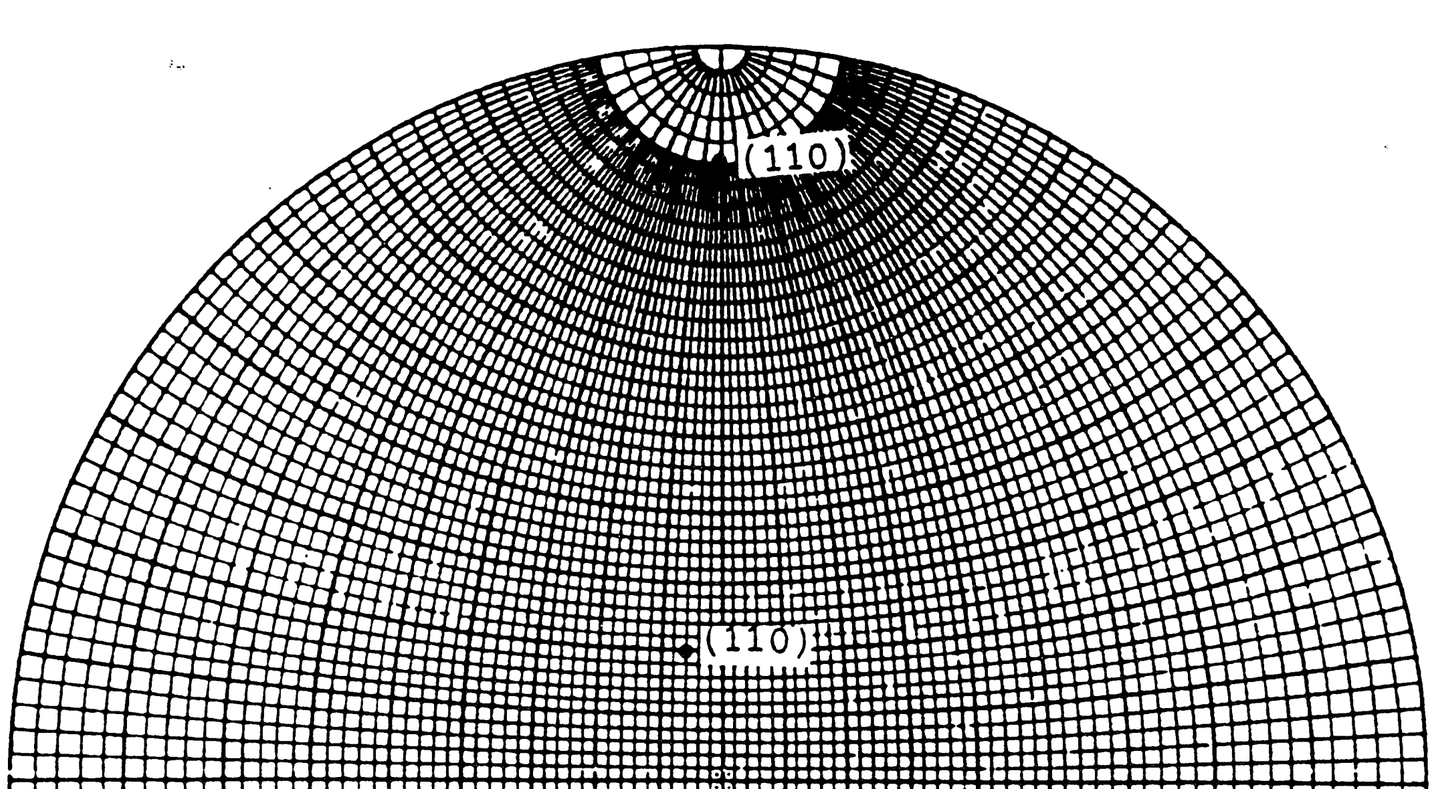

Figure 2.2.4 Stereographic projection of the bottom crystal in bicrystal B

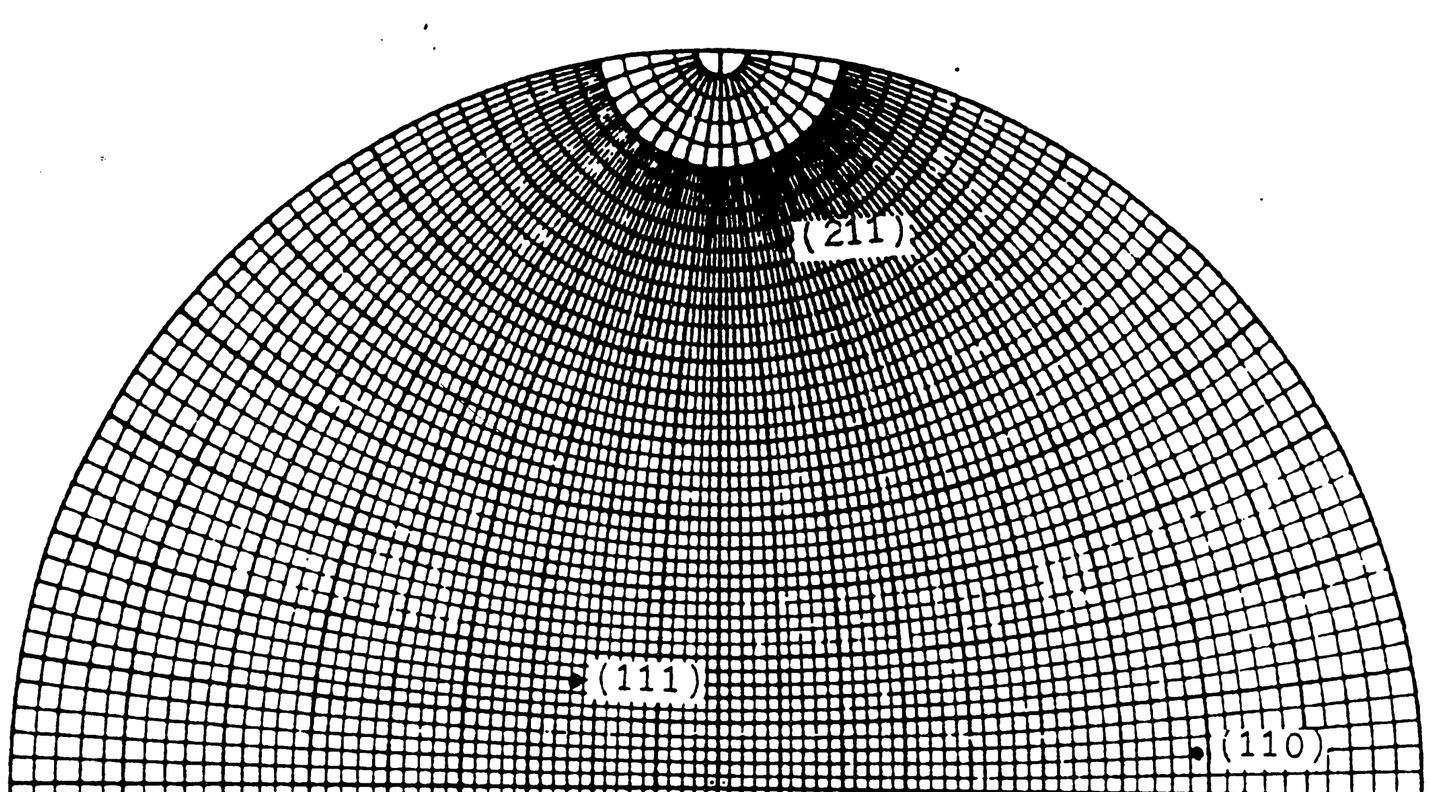

Figure 2.2.5 Stereographic projection of the top crystal in bicrystal C

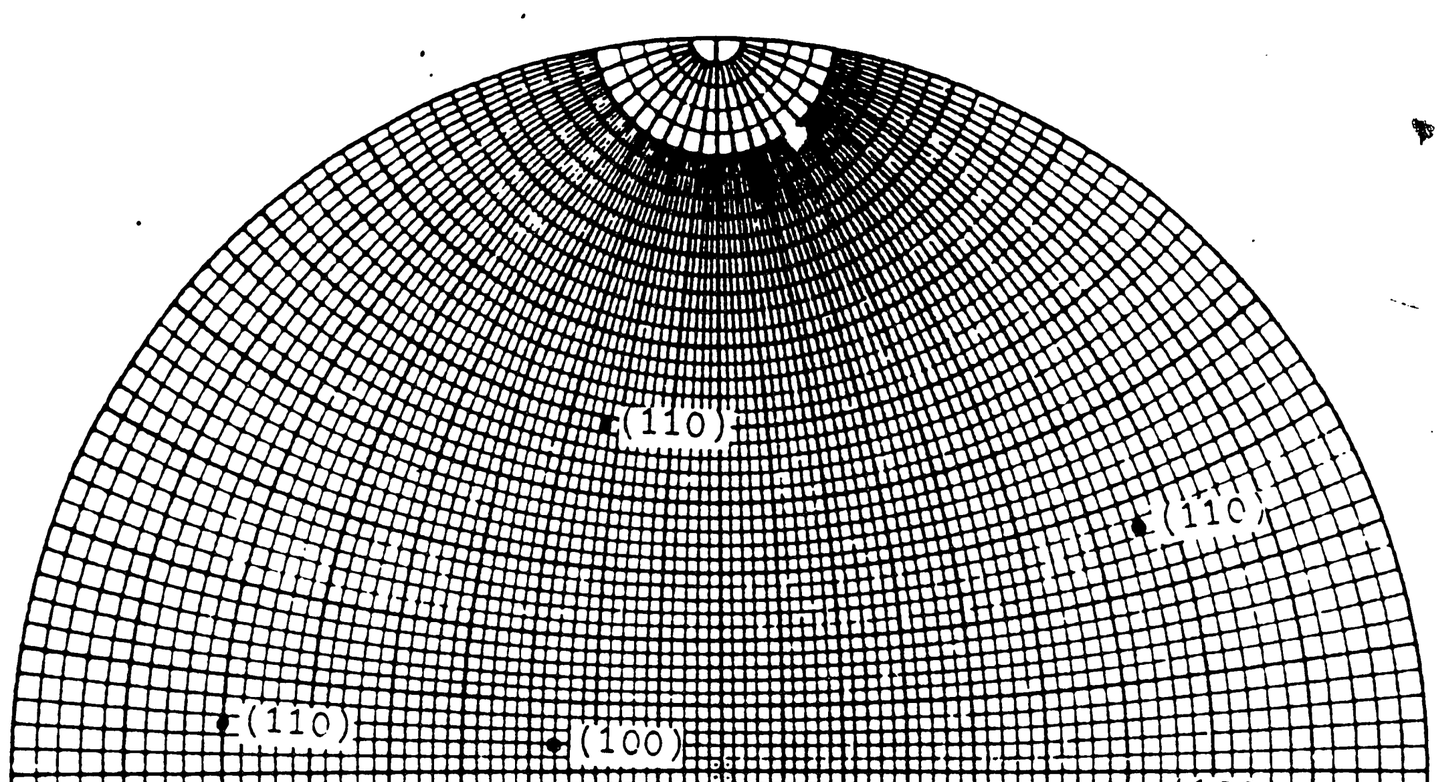

Figure 2.2.6 Stereographic projection of the bottom crystal in bicrystal C

between the top and bottom crystals in the bicrystal and a reference set of axes consisting of the beam axis, and axes perpendicular and parallel to the grain boundary. The axis of rotation, defined in the coordinate system of the top crystal by the unit vector u, was obtained by solving the eigenvector equation, [6]

$$([R] - [I])u = 0 .$$

Finally the equation

$$Tr\ [R] = 1 + 2\cos\chi$$

may be solved for the total rotation angle χ, [6].

The misorientation of two crystals in a bicrystal can also be described by a twist and a tilt angle. Twist and tilt angles are derived by splitting the single rotation χ about the axis u into two rotations about an axis parallel and an axis perpendicular to to the grain boundary. The angles of rotation about these axes are called the twist and tilt angles respectively. It can be shown that, [6]

$$\mathrm{Sin}\ \frac{\phi}{2} = \frac{\mathrm{Sin}\ \frac{\chi}{2}}{\sqrt{1 + \tan^2\alpha\ \cos^2\frac{\chi}{2}}}$$

and

$$\mathrm{Sin}\ \frac{\omega}{2} = \mathrm{Sin}\ \alpha\ \mathrm{Sin}\frac{\chi}{2}$$

where ϕ is the twist angle, ω is the tilt angle, χ is the

total rotation angle and α is the angle between u and the grain boundary normal.

Unfortunately the total rotation angle, as well as the twist and tilt angles are not unique. This ambiguity arises because there are 24 different misorientation matrices that can describe the same bicrystal. Each misorientation matrix has its own value of total rotation angle χ, rotation vector u, twist angle ϕ, and tilt angle ω. The other 23 rotation matrices, $[R_i]'$, can be calculated from the equation

$$[R_i]' = [P_i]\ [R]$$

where $[P_i]$ is a symmetry operation in matrix form and [R] is the original misorientation matrix. In the case of a cubic crystal there are three axes with four-fold symmetry, four axes with three-fold symmetry and six axes with two-fold symmetry, [7]. The four-fold axes are coincident with the crystal coordinate axes. Since there are three symmetry operations about each axis corresponding to a rotation angles of 90 degrees, 180 degrees and 270 degrees, the four-fold axes contribute nine rotation matrices. Similarly the three-fold axes, which are coincident with the body diagnals of a cubic crystal, each contribute two $[R]'$ matrices corresponding to rotation angles of 120 degrees and 240 degrees about each axis. Finally the two-fold axes located about the

six face diagnals of the cubic crystal contribute one new matrix each corresponding to a rotation of 180 degrees. Thus we have the original rotation matrix plus 23 degenerate martices calculated using the symmetry operations described above. Tables 2.2.1 through 2.2.6 show the 24 values of the total rotation angle and axis and the twist and tilt angle for each crystal.

χ	ϕ	ω
75.52	3.92	5.95
119.14	1.39	13.50
91.38	158.11	90.05
104.60	113.54	71.25
68.19	50.14	17.40
110.36	-156.55	0.00
180.00	80.95	107.81
118.95	2.54	24.71
155.92	5.67	66.04
180.00	30.19	124.69
101.71	29.65	61.18
158.10	-13.77	-57.14
143.13	73.46	32.75
180.00	34.00	124.11
75.74	6.69	18.29
152.99	10.69	125.63
180.00	3.59	126.72
127.21	4.73	88.70
139.05	11.07	46.01
95.80	-14.75	-87.77
113.08	-0.17	-1.04
150.34	-12.91	-22.60
115.94	103.73	152.52
119.97	-20.50	-26.77

Table 2.2.1 Total rotation angle χ, twist angle ϕ and tilt angle ω in degrees for specimen A

u_x	u_y	u_z
0.987	0.161	0.019
-0.674	-0.166	0.720
-0.415	0.872	0.261
0.703	0.202	0.682
0.365	0.526	0.768
0.381	0.853	0.357
0.200	-0.093	0.975
0.335	-0.458	0.824
-0.034	-0.507	0.861
-0.161	-0.508	0.846
0.531	-0.819	0.219
0.318	-0.347	0.882
0.681	0.409	0.607
-0.352	-0.431	0.831
0.648	-0.754	0.110
0.270	-0.491	0.828
-0.618	-0.121	0.777
0.011	-0.494	0.870
-0.658	0.197	0.727
-0.853	0.516	0.076
-0.799	0.294	0.525
0.608	-0.117	0.785
-0.191	-0.180	0.965
0.320	-0.931	0.176

Table 2.2.2 Components of rotation axis vector u for specimen A

χ	ϕ	ω
91.72	140.52	53.37
94.79	-10.90	-29.13
84.20	-82.58	-132.11
144.14	20.79	3.71
76.88	17.87	83.32
104.60	94.15	98.30
180.00	124.14	33.80
123.30	-122.53	-76.11
148.65	-13.14	-122.60
180.00	54.06	119.59
69.86	-2.06	-42.89
161.30	-59.16	-107.65
147.08	-147.08	-7.41
180.00	9.75	126.54
77.49	94.07	85.69
141.40	171.00	158.68
180.00	91.68	99.93
141.95	60.94	141.07
136.54	-77.95	-62.35
113.20	3.71	4.83
102.86	100.52	103.20
152.07	38.65	62.98
121.13	-8.55	-100.05
103.65	174.95	151.16

Table 2.2.3 Total rotation angle χ, twist angle ϕ and tilt angle ω in degrees for specimen B

u_x	u_y	u_z
0.847	0.423	0.322
-0.122	-0.613	0.780
-0.057	0.993	0.106
0.525	0.395	0.754
0.221	-0.913	0.343
0.142	0.945	0.294
0.497	-0.032	0.867
0.205	-0.288	0.936
-0.621	-0.480	0.620
-0.357	-0.456	0.815
-0.442	-0.701	0.559
-0.265	-0.458	0.849
0.585	0.328	0.742
-0.542	-0.476	0.693
0.835	-0.478	0.271
-0.255	-0.669	0.698
-0.275	-0.039	0.961
-0.262	-0.670	0.694
0.434	-0.479	0.763
0.612	-0.614	0.498
-0.962	0.269	0.045
0.044	-0.589	0.807
-0.695	-0.059	0.716
-0.181	-0.973	0.141

Table 2.2.4 Components of rotation axis vector u for specimen B

χ	ϕ	ω
90.14	41.84	120.56
137.94	-11.39	-11.73
87.45	-14.86	-25.56
100.40	-4.02	-6.42
157.74	-17.59	-33.89
175.95	0.56	0.91
180.00	99.59	92.07
180.00	117.65	60.08
94.56	-6.48	-16.69
64.25	76.90	27.87
107.54	-23.27	-34.72
117.21	89.16	98.28
99.64	-16.00	-48.76
91.68	144.95	39.30
180.00	90.05	101.30
100.97	17.07	18.66
144.87	-15.99	-12.77
83.09	-32.12	-75.23
136.17	-101.14	-71.90
117.42	104.65	48.79
126.41	22.89	36.09
118.91	17.14	20.56
106.71	1.49	5.87
75.37	-0.56	-1.23

Table 2.25 Total rotation angle χ, twist angle ϕ and tilt angle ω in degrees for specimen C

u_x	u_y	u_z
0.004	0.975	0.222
0.095	0.675	0.731
0.942	0.327	0.076
-0.297	-0.596	0.746
-0.428	-0.545	0.721
-0.454	-0.356	0.817
-0.413	0.249	0.876
-0.079	0.230	0.970
-0.941	0.329	0.076
0.738	-0.105	0.666
0.371	0.828	0.419
0.987	-0.138	0.079
-0.713	0.113	0.692
0.361	0.343	0.867
-0.074	-0.796	0.601
0.466	0.719	0.515
-0.175	0.201	0.964
-0.685	0.002	0.728
-0.115	0.466	0.877
-0.001	-0.226	0.974
0.116	-0.843	0.525
-0.248	0.485	0.839
-0.805	0.579	0.134
0.540	0.820	0.190

Table 2.2.6 Components of rotation axis vector u for specimen C

Since each degenerate rotation matrix has its own value for u, χ, ϕ and ω, there is some ambiguity about which rotation matrix should be chosen to represent the bicrystal. Lange [6] proposes that the rotation martix that produces the lowest total rotation angle χ be chosen. Following this convention the resultant angles for each bicrystal are presented in tables 2.2.7 and 2.2.8. Table 2.2.7 shows the rotation, twist and tilt angles for each bicrystal, while Table 2.2.8 shows the components of rotation axis vector u in the reference coordinate system for each bicrystal.

Bicrystal	Total Rotation Angle χ in Degrees	Twist Angle ϕ in Degrees	Tilt Angle ω in Degrees
A	68.2	50.1	7.4
B	69.9	-2.1	-42.9
C	64.25	76.9	27.9

Table 2.2.7 Final total rotation,twist and tilt angles

Bicrystal	Rotation axis vector u		
	X component	Y component	Z component
A	.99	.16	.02
B	-.44	-.70	.56
C	.74	-.17	.67

Table 2.2.8 Final rotation axis vectors

Chapter 3 Error Estimates

Three sources of experimental uncertainty which could lead to scatter in the failure time data were considered. They were the uncertainty in the applied stress, the uncertainty in the temperature, and the effects of eccentric loading. In this chapter the error in the failure time data caused by these three sources will be estimated.

3.1 Uncertainty in failure time due to uncertainty in the applied stress

The principal contributors to the total load are the applied load, the load due to the pressure of the argon gas in the bellows and the load due to the weight of the cooling water in the cooling fixture on the lower pull rod. Each of these loads has a nominal value and an uncertainty associated with it. The uncertainty in the applied load was estimated to be 0.5 newtons. The uncertainty in the argon pressure load was estimated at .32 newtons and the uncertainty in the cooling water load was estimated at .04 newtons. Assuming that the uncertainties have a normal (Gaussian) distribution, they may be added in quadrature, [8], to obtain

$$\delta_t = \sqrt{\sum_{i=1}^{n} \delta^2_i}$$

where

δ_t = total uncertainty

δ_i = contributions to the total uncertainty

This yields a total uncertainty of .60 newtons. Assuming a nominal cross-sectional area of 7.94 mm^2, the uncertainty in the applied load causes an uncertainty in the applied stress of .075 MPa.

Variations in the diameter of the specimen also contribute to the uncertainty in the applied stress. From direct measurement, the variation of the specimen diameter was determined to be 2.54×10^{-2} mm. This caused an uncertainty in the area of .127 mm^2. The resulting uncertainty in the applied stress is given by, [8]

$$\delta\sigma = \left| \frac{-P}{A^2} \right| \delta A$$

where

$\delta\sigma$ = uncertainty in the stress

P = the nominal total applied load

A = nominal area of the specimen

δA = uncertainty in the area

The total uncertainty in the applied stress was found by combining in quadrature the uncertainty in the stress due

to the uncertainty in the applied load and the uncertainty in the stress due to variation in the specimen's diameter.

To evaluate the uncertainty in the failure times due to the uncertainty in the stress, the following empirical relationship was employed

$$t_f = \frac{K}{\sigma^n}$$

where

σ = the applied stress

t_f = failure time

K,n = constants

For the high stress experiment, group A, the constants K and n were determined by writing the the above equation in the form

$$Ln(\bar{t}_f) = nLn(\sigma)+Ln(K)$$

where

$\bar{t}_f$ = mean failure time of the specimens tested at each stress level

and then performing a least squares fit utilizing the data from all three specimen groups. The results of this analysis were n=1.70 and $K=6.97\times10^3(MPa)^n$ Hrs. The constants for the two lower stress experiments, groups B and C, were found using only the stress and mean failure

time data for these two groups. This analysis yielded the values n=1.56 and K=5.94 x 10^3(MPa)^n Hrs. The uncertainty in the failure times can then be calculated from

$$\delta t_f = \left| \frac{-n\ K}{\sigma^{(n+1)}} \right| \delta\sigma$$

where

δt_f = uncertainty in the failure time

$\delta\sigma$ = uncertainty in the applied stress

Table 3.1.1 displays the total uncertainty in the applied stress and the resulting uncertainty in the failure time for each specimen group.

specimen group	stress uncertainty (MPa)	failure time error (hrs)
A	.123	11.3
B	.087	116.7
C	.097	29.2

Table 3.1.1 Error in failure time error due to uncertainty in the applied stress

3.2 Uncertainty in failure time due to variations in temperature

The uncertainty in the temperature was estimated to

be ±1°C. This figure is based on the claims of the manufacturer and measurements made during operation. The uncertainty in the failure times due to the variation in temperature was calculated assuming an Arhenius-type dependance of failure time upon temperature i.e.,

$$t_f = f(\sigma) \exp\left(\frac{Q}{RT}\right)$$

where

t_f = failure time

$f(\sigma)$ = function of the applied stress

Q = activation energy

R = universal gas constant

T = temperature

Differentiating to find the uncertainty in the failure times yields the equation,

$$\delta t_f = \left| \frac{f(\sigma)Q}{RT^2} \exp\left(\frac{Q}{RT}\right) \right| \delta T$$

and rearranging

$$\frac{\delta t_f}{t_f} = \frac{Q}{RT} \frac{\delta T}{T}$$

where

δT = the uncertainty in the temperature

Substituting in the values,

$$Q = 47.12 \text{ Kcal/mol}$$

$$R = .001987 \text{ Kcal/mol K}$$

$$T = 875.15^{\circ} \text{ K}$$

$$\delta T = 1^{\circ} \text{ K}$$

reduces the equation to,

$$\delta t_f = .031\ t_f$$

Therefore the uncertainty in the failure times for groups A, B and C due to the uncertainty in the temperature are 10.4 hrs, 56.7 hrs and 22.7 hrs respectively.

3.3 Uncertainty in failure times due to eccentric loading

Eccentric loading occurs when the resultant of the load P is not applied along the axis of the cylindrical specimen. The distance between the point of application of the resultant load and the center of the specimen is called δ. Eccentric loading produces a bending moment of magnitude $P\delta$ and hence produces a non-uniform stress distribution over the specimen cross-section. In order to estimate the effect of the eccentric loading on the failure times, a non-linear analysis was performed to calculate the resulting stress distribution.

The non-linear analysis begins by assuming power law behavior in creep i.e.,

$$\dot{\epsilon} = C\sigma|\sigma|^{n-1} + \frac{\dot{\sigma}}{E} \qquad (1)$$

where

$\dot{\epsilon}$ = strain rate

C = constant

σ = stress

$\dot{\sigma}$ = stress rate

n = constant

E = Young's modulus

We assume that the total axial strain rate is the sum of a uniform axial component plus a linearly varying bending strain.

$$\epsilon = \epsilon_a + K(t)y \qquad (2)$$

where

ϵ = total axial strain

ϵ_a = uniform axial strain

K(t) = time varying curvature

y = distance from the centerline

Differentiating with respect to time, we obtain

$$\dot{\epsilon} = \dot{\epsilon}_a + \dot{K}(t)y \qquad (3)$$

We now assume steady-state conditions which imply that $\dot{\sigma}=0$ and $\dot{\epsilon}_a$ and $\dot{K}$ are constants. Then, equating equation (1) with equation (3) and solving for σ with the

assumption $\sigma > 0$, yields

$$\sigma = \left(\frac{\dot{\epsilon}_a + \dot{K}y}{C}\right)^{\frac{1}{n}} \qquad (4)$$

From simple considerations of mechanical equilibrium,

$$-P\delta = \int_A \sigma y \, dA \qquad (5)$$

and

$$P = \int_A \sigma dA \qquad (6)$$

Substituting yields

$$-P\delta = \int_A \left(\frac{\dot{\epsilon}_a + \dot{K}(t)y}{C}\right)^{\frac{1}{n}} y dA \qquad (7)$$

and

$$P = \int_A \left(\frac{\dot{\epsilon}_a + \dot{K}(t)y}{C}\right)^{\frac{1}{n}} dA \qquad (8)$$

To calculate these integrals over a circular cross-section of radius a ,dA is replaced by

$$dA = 2\sqrt{a^2 - y^2}\, dy \qquad (9)$$

Substituting equation (9) into equations (7) and (8) and rearranging yields

$$\int_{-a}^{a} \left(\dot{\epsilon}_a + \dot{K}y\right)^{\frac{1}{n}} y\sqrt{a^2 - y^2}\, dy = -\frac{1}{2}P\delta C^{\frac{1}{n}} \quad (10)$$

and

$$\int_{-a}^{a} \left(\dot{\epsilon}_a + \dot{K}y\right)^{\frac{1}{n}} \sqrt{a^2 - y^2}\, dy = \frac{1}{2}PC^{\frac{1}{n}} \quad (11)$$

Non-dimensionalizing (10) and (11) by letting $\rho = \frac{y}{a}$ leads to the equations

$$\int_{-1}^{1} \left(\dot{\epsilon}_a + \dot{K}a\rho\right)^{\frac{1}{n}} \rho \sqrt{1 - \rho^2}\, d\rho = \frac{-P}{2a^2}\left(\frac{\delta}{a}\right) C^{\frac{1}{n}} (11)$$

and

$$\int_{-1}^{1} \left(\dot{\epsilon}_a + \dot{K}a\rho\right)^{\frac{1}{n}} \sqrt{1 - \rho^2}\, d\rho = \frac{P}{2a^2} C^{\frac{1}{n}} \quad (12)$$

Equations (11) and (12) constitute two non-linear equations of the form

$$F(\dot{\epsilon}_a, \dot{K}) = 0 \quad (13)$$

and

$$G(\dot{\epsilon}_a, \dot{K}) = 0 \quad (14)$$

Values for $\dot{\epsilon}_a$ and $\dot{K}$ are obtained by applying Newton's method to equations (13) and (14) and using six-point Gaussian integration to evaluate the required integrals. The starting values of $\dot{\epsilon}_a$ and $\dot{K}$ for this iterative

process were taken to be the values of $\dot{\epsilon}_a$ and $\dot{K}$ with no eccentric loading; i.e.,

$$\dot{K} = 0$$

and

$$\dot{\epsilon}_a = C\left(\frac{P}{\pi a^2} \right)^n$$

For the load train used in the labratory the loading eccentricity was estimated to be 2.5% of the specimen radius with an uncertainty of another 2.5% of the specimen radius. Hence a maximum eccentricity of 5.0% was used for this analysis. The values for n and C were taken to be 4.8 and $5.83 \times 10^{-41} sec^{-1}(Pa)^{-n}$ respectively [9].

Once values for $\dot{K}$ and $\dot{\epsilon}_a$ are found, they may be substituted into equation (4) to find the stress distribution. The additional stress due to the eccentric loading can then be conservatively estimated by subtracting the maximum stress at the outer edge of the specimen from the nominal stress. This additional stress is then treated as an uncertainty in the applied stress, and the uncertainty in the failure times due to eccentric loading may be calculated the same way as the uncertainty in the failure times due to the other uncertainties in applied stress were calculated. Table 3.3.1 shows the results of the Newton's method, $\dot{\epsilon}_a$ and $\dot{K}$, along with the

additional stress in the specimen for each stress level and the resulting uncertainty in the time to failure data.

Specimen Group	Stress (MPa)	$\dot{K} \times 10^{-5}$ ($s^{-1}m^{-1}$)	$\dot{\epsilon}_a \times 10^{-8}$ (s^{-1})	Add. Stress (MPa)	δt_f (Hrs.)
A	6.06	-1.18	2.25	0.92	84.1
B	2.13	-7.90	0.015	0.33	442.8
C	3.82	-1.28	0.245	0.58	174.5

Table 3.3.1 Results of eccentric loading analysis

Since the uncertainty in the eccentricity is only 2.5% of the specimen radius, the uncertainty in the failure times due to eccentric loading is only half the value that appears in table 3.3.1. Summing in quadrature the failure time error contributions from the three sources of experimental uncertainty considered yields the final results, which are summarized in table 3.3.2.

specimen group	stress level (MPa)	failure time error (hrs)
A	6.06	44.8
B	2.13	229.1
C	3.82	94.8

Table 3.3.2 Error analysis results

Chapter 4 Results

Failure time data, Weibull plots of the failure time data, represenative micrographs of the fracture surface and a Weibull plot of the area of the creep cavities will be presented in this chapter.

4.1 Failure times

Tables 4.1.1 through 4.1.3 show the applied stress and the failure time of each specimen tested to date. As noted previously all specimens were tested at 600 ℃.

Specimen	Stress (MPa)	Failure Time (hrs)
A1	6.06	300.2
A2	6.06	313.0
A3	6.06	357.1
A4	6.06	359.8
A5	6.06	194.6
A6	6.06	326.4
A7	6.06	331.4
A8	6.06	358.1

Table 4.1.1 Failure times for specimen group A

Specimen	Stress (MPa)	Failure Time (hrs)
B1	2.13	2230.5
B2	2.13	836.2
B3	2.13	2058.0
B4	2.13	2013.5
B5	2.13	1195.6
B6	2.13	1235.6
B7	2.13	3241.5

Table 4.1.2 Failure times for specimen group B

Specimen	Stress (MPa)	Failure Time (hrs)
C1	3.82	586.9
C2	3.82	172.6
C3	3.82	1203.3
C4	3.82	258.8
C5	3.82	630.6
C6	3.82	1078.7
C7	3.82	1157.9
C8	3.82	770.7

Table 4.1.3 Failure times for specimen group C

4.2 Weibull analysis

Figure 4.2.1 shows failure time for each test series plotted on Weibull paper. It can be seen that the two paramater Weibull distribution offers a reasonably good fit to the distribution of failure times. Also shown is the maximum likelyhood estimation (MLE) fit to each test series,[10]. The two-parameter Weibull distribution has the form

$$F(x) = 1 - \exp\left(-\left(\frac{x}{\beta}\right)^{\rho}\right)$$

The Weibull parameters obtained from the MLE fit to each series are presented in table 4.4.1.

Specimen Group	β (units)	ρ (units)
A	336.3	9.67
B	2249.3	2.87
C	855.5	2.21

Table 4.4.1 Weibull Parameters for each test series

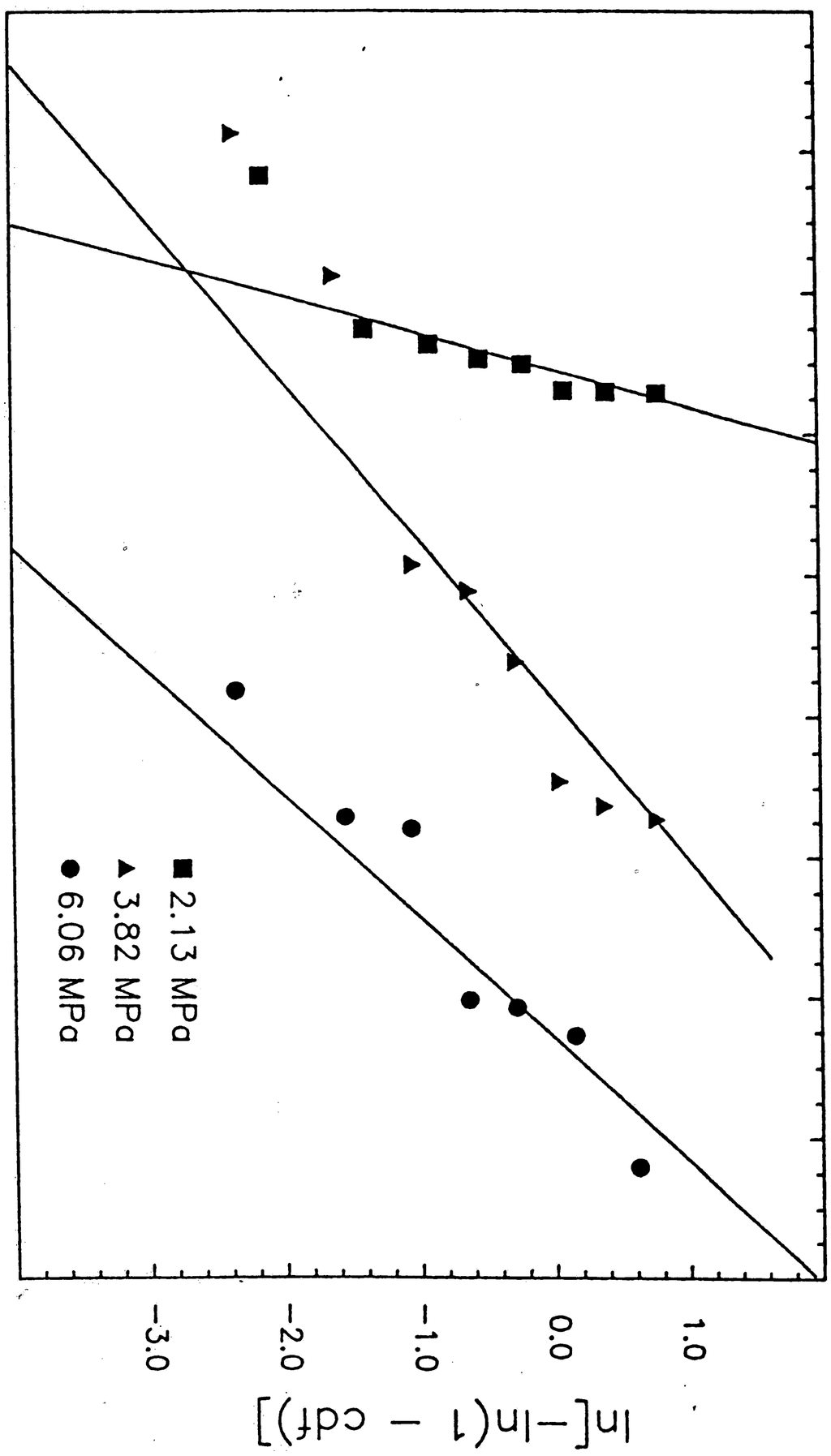

Figure 4.2.1 Weibull plots of the failure time data

4.3 Fracture surfaces

After failure, the fractured surface of each specimen was examined using an ETEC Autoscan scanning electron microscope. Micrographs produced with the scanning electron microscope yield interesting insights into the failure mechanisms. Figure 4.3.1 shows the fracture surface of specimen of A3. Here we observed a fairly large ductle failure region extending over about one half of the specimen, with the remainder of the surface covered with creep cavities. This pattern is common to the specimens tested at the highest stress level. In sharp contrast, the specimen tested at the lowest stress level were found to have large cavitated areas and a relatively small ductle failure regions. The fracture surface in figure 4.3.2 illustrates this point.

The creep cavities on the fracture sruface of each specimen differed in size and shape from specimen to specimen and from area to area on a fracture surface. Figures 4.3.3 through 4.3.5 show some represenative creep cavities.

Figure 4.3.1 Fracture surface of specimen A3

Figure 4.3.2 Fracture surface of specimen B7

Figure 4.3.3 creep cavities from specimen B1

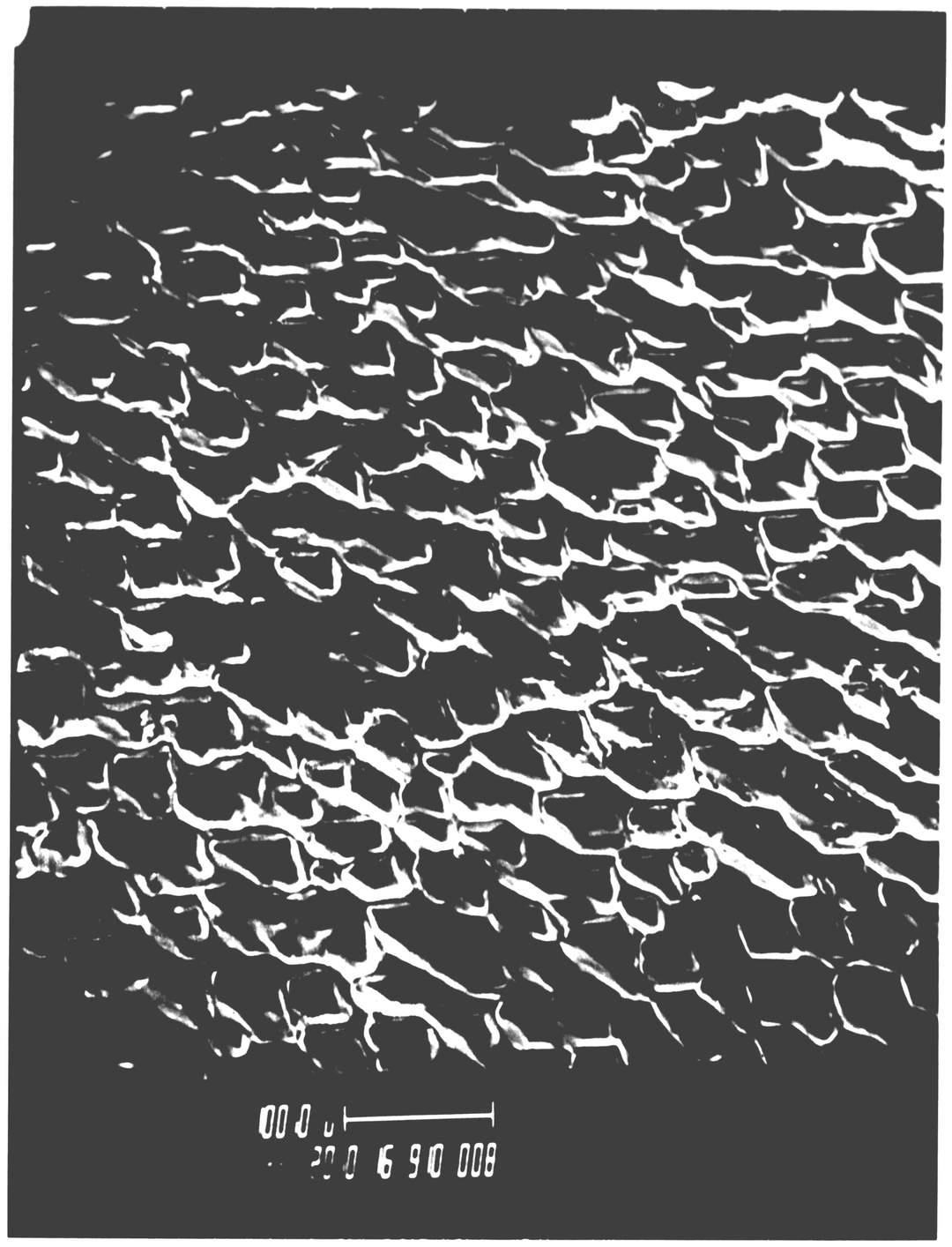

Figure 4.3.4 Creep cavities from specimen B1

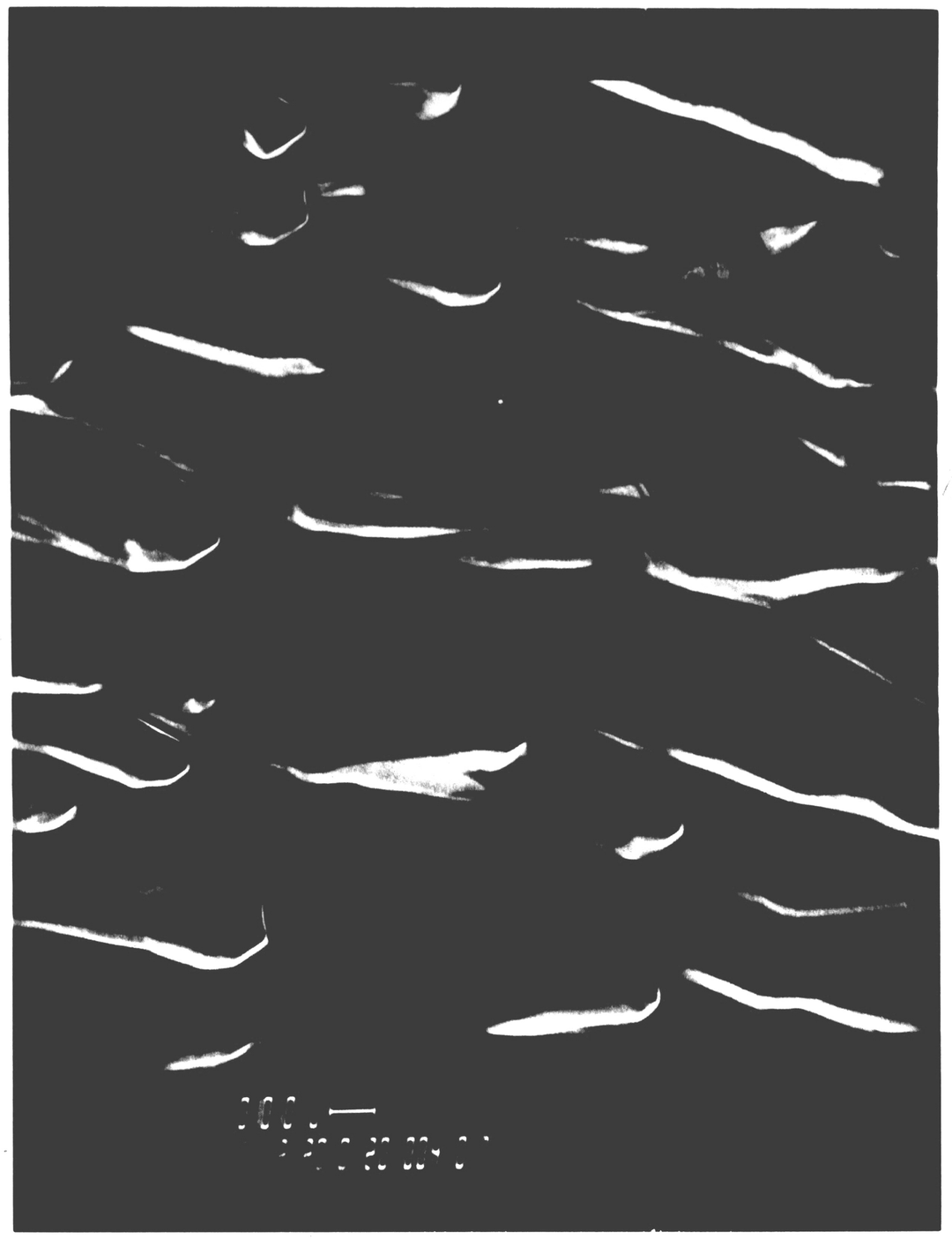

Figure 4.3.5 Creep cavities from specimen C1

4.4 Image analysis

A number of micrographs similar to figures 4.3.3 through 4.3.5 were analyzed at the National Bereau of Standards in Washington D.C.. An image analysis was performed using a Bausch and Lomb Omnicon. Since the Omnicon could not distinguish the cavity edges on the original micrographs, acetate tracings of the micrographs were analyzed. The area of each cavity was determined and a Weibull plot of the area was produced for each micrograph analyzed. Figure 4.4.1 shows a typical Weibull plot.

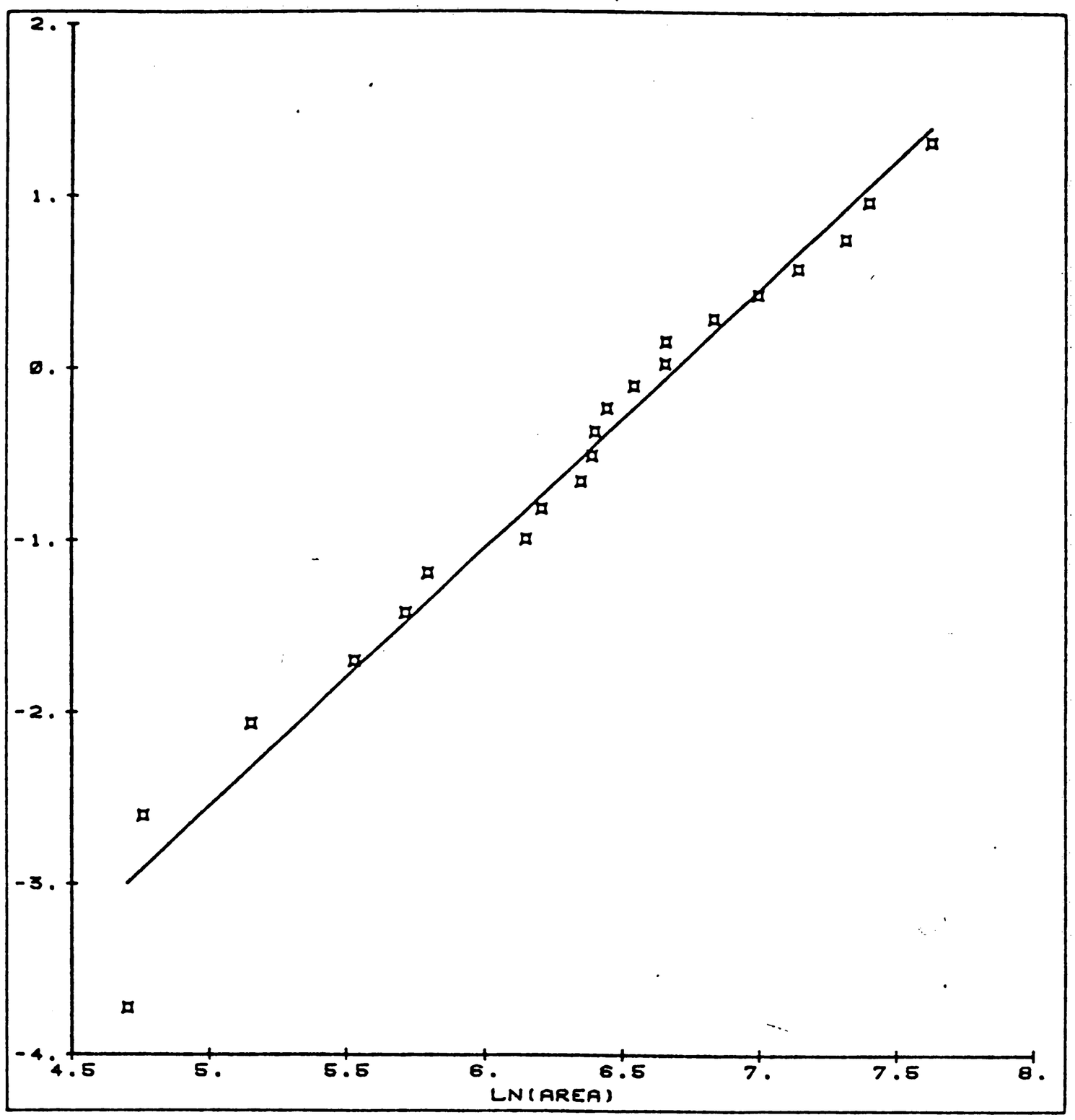

Figure 4.4.1 Weibull plot of the area ofcavities from specimen A2

Chapter 5 Conclusions

The most important conclusion that can be drawn from these experiments is that creep rupture, caused by intergranular cavitation, contains a substantial stochastic component. This is easily seen in the large scatter in the failure time data for groups B and C. Group B had a mean failure time of 1,830 hrs. with a high and low failure times of 3,241 hrs. and 836 hrs. Group C had a mean failure time of 732 hrs. with high and low failure times of 1203 hrs. and 173 hrs. The experimental error, as calculated in chapter 3, for specimen groups B and C is ±229 hrs and ±95 hrs., respectively. By comparing the high and low failure times with the estimated experimental error it is obvious that the experimental error accounts for only a small fraction of the observed scatter in the failure times for groups B and C. Therefore almost all of the scatter in the data must be attributed to the stochastic component of the intergranular creep rupture process.

Specimen group A, on the other hand, showed much less scatter. Its mean failure time was 335 hrs. with a high and low times of 195 hrs. and 360 hrs. The experimental error, in this case ±45 hrs., covers almost all of the scatter in the failure time data. The absence of stochastic behavior in the failure times in this test

series can be attributed to the predominantly ductle-rupture failure mode observed in specimens in group A. The dominance of the ductle-rupture failure mode, an essentially deterministic failure mode, is illustrated in the micrographs of the fracture surfaces of group A specimens. From these results we conclude that the probabilistic feature of the creep rupture process will only be seen in experiments in wich creep cavitation is the dominant failure mode.

This research has also shown that the two parameter Weibull distribution fits the failure time data for all three test series well. It is also very interesting to note that the scatter in the two test series at the lower stress levels, as measured by the slope of the Weibull fit are approximately the same.

Finally the statistical distribution of the cavity areas on the fracture surface was also found to have a Weibull fit. This result is in qualitative agreement with analytic results obtained by Fariborz, Harlow and Delph [11].

References

[1] E. Lister et al., "Determination of Elevated Temperature Properties of Steel", in Proc. Joint Conf. on High-Temperature Properties of Steels, pp.47-60, British Irom and Steel Research Assn. and Iron and Steel Inst., Eastbourne (1966).

[2] W. Rutman, M. Krause, and K. J. Kremer, "International Community tests on Long-Term Behavior of 2 1/4 Cr - 1 Mo Steel", in Proc. Joint Conf. on High-Temperature Properties of Steels, pp. 23-29, British Irom and Steel Research Assn. and Iron and Steel Inst., Eastbourne (1966).

[3] D. R. Hayhurst, "The Effects of Test Variables on Scatter in High-Temperature Tensile Creep-Rupture Data", Int. J. Mech. Sci., Vol 16, pp.829-841 (1974).

[4] F. Garofalo, R. W. Whitmore, and W. F. Domis, "Creep and Creep-Rupture Relationships in an Austinitic Stainless Steel", Trans. AIME, Vol. 21 pp. 310-319 (1961).

[5] B. D. Cullity, Elements of X-Ray Diffraction, Addison--Wesley Publishing, London (1978).

[6] F. F. Lange, "Mathematical Characterization of a General Bicrystal", Acta Metall., Vol. 15, pp 311-319 (1967).

[7] C. S. Pande and Y. T. Chou, "Growth, Structure, and

Mechanical Behavior of Bicrystals", in Treatise on Materials Science and Technology, pp. 43-53, Academic Press, New York (1975).

[8] J. R. Taylor, An Introduction to Error Analysis, University Science Books, California (1982).

[9] H. Frost and M. Ashby, Deformation-Mechanism Maps: The Plasticity of Creep of Metals and Ceramics, Pergamon Press, New York (1982).

[10] D. Graupe, Identification of Systems, Kieger Publishing, Florida (1972).

[11] S. J. Fariborz, D. G. Harlow and T. J. Delph, "The Effects of Nonperiodic Void Spacing Upon Intergranular Creep Cavitation", Acta Metall., Vol 33, pp. 1-9 (1985)

Vita

John Farris was born in Hartford, Connecticut on September 18, 1964 to Paul and Paullette Farris. He attended public school in South Windsor, Connecticut, graduating from South Windsor High in June of 1982. His undergraduate education consisted of one year at Drexel University and the remaining three years of study at Lehigh University. John Farris received his Bachelor of Science Degree in Mechanical Engineering from Lehigh University in January of 1987.